Title	Modelling TiO 2 formation in a stagnation flame using method of moments with interpolative closure
Author(s)	Manuputty, Manoel Y.; Akroyd, Jethro; Mosbach, Sebastian; Kraft, Markus
Citation	Manuputty, M. Y., Akroyd, J., Mosbach, S., & Kraft, M. (2017). Modelling TiO2 formation in a stagnation flame using method of moments with interpolative closure. Combustion and Flame, 178,135-147.
Date	2017
URL	http://hdl.handle.net/10220/44523
Rights	© 2017 The Combustion Institute (published by Elsevier). This is the author created version of a work that has been peer reviewed and accepted for publication in Combustion and Flame, published by Elsevier on behalf of The Combustion Institute. It incorporates referee's comments but changes resulting from the publishing process, such as copyediting, structural formatting, may not be reflected in this document. The published version is available at: [http://dx.doi.org/10.1016/j.combustflame.2017.01.005].

Modelling TiO_2 formation in a stagnation flame using method of moments with interpolative closure

Manoel Y. Manuputty[a], Jethro Akroyd[a], Sebastian Mosbach[a], Markus Kraft[a,b,*]

[a] *Department of Chemical Engineering and Biotechnology, University of Cambridge, New Museums Site, Pembroke Street, Cambridge, CB2 3RA, United Kingdom*
[b] *School of Chemical and Biomedical Engineering Nanyang, Technological University, 62 Nanyang Drive, 637459, Singapore*

Abstract

The stagnation flame synthesis of titanium dioxide nanoparticles from titanium tetraisopropoxide (TTIP) is modelled based on a simple one-step decomposition mechanism and one-dimensional stagnation flow. The particle model, which accounts for nucleation, surface growth, and coagulation, is fully-coupled to the flow and the gas phase chemistry and solved using the method of moments with interpolative closure (MoMIC). The model assumes no formation of aggregates considering the high temperature of the flame. In order to account for the free-jet region in the flow, the computational distance, $H = 1.27$ cm, is chosen based on the observed flame location in the experiment (for nozzle-stagnation distance, $L = 3.4$ cm). The model shows a good agreement with experimentally measured mobility particle size for stationary stagnation surface with varying TTIP loading, although the particle geometric standard deviation, GSD, is underpredicted for high TTIP loading. The particle size is predicted to be sensitive to the sampling location near the stagnation surface in the modelled flame. The sensitivity to the sampling location is found to increase with increasing precursor loading and stagnation temperature. Lastly, the effect of surface growth is evaluated by comparing the result with an alternative reaction model. It is found that surface growth plays an important role in the initial stage of particle growth which, if neglected, results in severe underprediction of particle size and overprediction of particle GSD.

Keywords: Titanium dioxide, nanoparticle, TTIP, particle dynamics, method of moments, stagnation flame

*Corresponding author
Email address: mk306@cam.ac.uk (Markus Kraft)

1. Introduction

Titanium dioxide (TiO_2) is a material with wide industrial applications. It exists mainly as anatase and rutile polymorphs. Anatase is used in photocatalysis and photovoltaic applications due to its photoactivity while rutile is mainly used in white pigment due to its high refractive index. Pigment is the single greatest use of titanium worldwide with annual global production of 7.2 million tonnes of TiO_2 in 2015 [1]. For many applications, including pigments, the ability to control the nanoparticle properties, for example size distribution and crystallinity, is critical to the performance of the material.

Despite its commercial importance, a complete understanding of the formation of titanium dioxide, also known as titania, is still lacking. One of the main manufacturing processes is the chloride process, which uses titanium tetrachloride ($TiCl_4$) as the presursor. The main difficulty lies in the fact that the chloride process involves harsh reaction conditions at high temperature which limit the ability to perform experimental analysis. The experimental studies are further complicated by the inherent challenges in nanoscale characterization. Computational modeling offers attractive capabilities to investigate such systems and combined with well designed experimental work, to provide insights into the particle formation [2–8].

Another common precursor of TiO_2 is titanium tetraisopropxide (TTIP). TTIP is often preferred as an alternative to $TiCl_4$ for lab-scale studies because it is more stable and easier to handle. A number of works have combined experimental studies and computational tool, in particular population balance modelling, in order to investigate how the various processes like nucleation, surface growth, coagulation and coalescence affect the particle properties in TTIP-TiO_2 system [9–12].

Tsantilis et al. [9] solved a population balance model with different reaction models and compared the results with experimental data from a premixed methane-oxygen flat flame. They found that the reaction model which includes surface growth is most consistent with the experimental data, especially near the burner face (< 1 cm) and so concluded that surface reaction is an important growth mechanism. However, they observed that further away from the burner, neglecting surface growth also yielded a good agreement with experimental data because coagulation was already dominant. This suggests that surface growth is dominant in the early stage of particle formation while coagulation in later stages.

The importance of coagulation was also observed by Zhao et al. [11] using a burner-stabilized stagnation flame (BSSF) with embedded aerosol sampling probe. The experimental data was compared with a population balance model solved with a sectional method. They observed that the high residence time in the experiment resulted in large aggregate structure with relatively broad particle size distribution. In another study, Yu et al. [12] compared the experimental data from a diffusion flame reactor and the particle model solved with a quadrature method of moments (QMoM). They showed that higher particle residence time in the high temperature zone led to formation of irregular agglomerates.

Tsantilis and Pratsinis [10] showed theoretically that limiting particle residence time (or freezing the particle growth) is necessary in order to produce particles with narrow size distribution. Such operating conditions can be achieved by either quenching in critical flow nozzles [13] or using impinging jets on stagnation plate [14–16].

Tolmachoff et al. [14] introduced a flame stabilized on rotating surface (FSRS) technique to produce TiO_2 nanoparticles with narrow size distribution. In this method, a TTIP-doped premixed $C_2H_4/O_2/Ar$ jet impinges on a rotating stagnation surface which acts as a substrate holder. A flat flame is formed and stabilized very close to the stagnation surface due to the high jet velocity, confining the high temperature zone within 3-4 mm from the surface. The surface is cooled by forced convection, resulting in a high temperature gradient which facilitates particle deposition by thermophoresis. As a result of the small combustion zone very near to the stagnation surface, particle growth is quenched at early stage leading to particle size distribution narrower than the self-preserving distribution [17]. More importantly, the particle properties including size distribution and crystallinity were shown to be able to be controlled by varying the experimental conditions including stagnation temperature and precursor loading. Korobeinichev et al. [18] also used a similar technique to produce crystalline TiO_2 with narrow size distribution from a TTIP-doped $H_2/O_2/Ar$ flame.

In addition to the ability to produce crystalline nanoparticles or films for various applications [15, 19], the features of FSRS offer the ability to study early particle formation of TiO_2 from TTIP. This could be used to improve our understanding of chemical decomposition of TTIP and the reactions leading to the formation of TiO_2. It also provides data against which to assess the detailed mechanisms, for example those proposed by Buerger et al. [20] and Shmakov et al. [21].

Previous studies have modelled similar flames without particles [14, 16, 18] while others introduced the particle formation in post-processing [11]. Modak et al. [22] attempted to couple the gas-phase and particle model using a BSSF configuration and sectional method, but ignored the effect of surface growth which has been shown to be critical by earlier studies.

The purpose of this paper is to implement a particle model employing a simple reaction mechanism available in literature and to demonstrate the ability to model TiO_2 formation from TTIP in FSRS. The predicted results are compared with experimental data obtained from Tolmachoff et al. [14]. This work aims to investigate the effects of varying important process parameters, including precursor loading and stagnation temperature, and to explain experimentally observed trends of particle size in terms of relative rates of the particle processes modelled. In particular, we aim to understand the role of surface reaction in particle growth in the FSRS experiment.

2. Model description

2.1. Flow model

The flow in the burner was assumed to be an axisymmetric stagnation flow. It was modelled using pseudo one-dimensional approximation, illustrated in Fig. 1, by introducing a streamfunction of the form

$$\Psi(z,r) = r^2 U(z), \tag{1}$$

where z is the axial distance from the nozzle, r is the radial distance from the burner centerline, and $U(z)$ is the axial component of the streamfunction. The axial velocity, u_z, and radial velocity, u_r, are given by

$$u_z = \frac{2U(z)}{\rho} \tag{2}$$

$$u_r = -\frac{r}{\rho}\frac{\mathrm{d}U(z)}{\mathrm{d}z}, \tag{3}$$

where ρ is the gas mixture density.

By introducing the streamfunction assumption, the Navier-Stokes equations are reduced to a set of one-dimensional ordinary differential equations [more on derivation in 23],

$$\frac{\mathrm{d}\Lambda}{\mathrm{d}z} = 0 \tag{4}$$

$$\Lambda - 2\frac{\mathrm{d}}{\mathrm{d}z}\left(\frac{UG}{\rho}\right) + \frac{3G^2}{\rho} + \frac{\mathrm{d}}{\mathrm{d}z}\left[\mu\frac{\mathrm{d}}{\mathrm{d}z}\left(\frac{G}{\rho}\right)\right] = 0, \tag{5}$$

where Λ is the radial pressure-gradient eigenvalue, G is $\mathrm{d}U/\mathrm{d}z$, and μ is the gas mixture viscosity. Equations (4) and (5) are the eigenvalue and momentum equations for one-dimensional stagnation flow, respectively. Next, assuming the temperature, T, and the species mole fractions, Y_k, are radially independent, the additional governing equations for T and Y_k are given as

$$2U\frac{\mathrm{d}T}{\mathrm{d}z} - \frac{1}{c_p}\frac{\mathrm{d}}{\mathrm{d}z}\left(\lambda\frac{\mathrm{d}T}{\mathrm{d}z}\right) + \frac{\rho}{c_p}\sum_{k=1}^{K} Y_k c_{p,k} V_k \frac{\mathrm{d}T}{\mathrm{d}z} + \frac{1}{c_p}\sum_{k=1}^{K} h_k \dot{\omega}_k + \frac{1}{c_p}\dot{Q}_{\mathrm{rad}} = 0 \tag{6}$$

$$2U\frac{\mathrm{d}Y_k}{\mathrm{d}z} + \frac{\mathrm{d}}{\mathrm{d}z}(\rho Y_k V_k) - W_k\dot{\omega}_k = 0 \quad (k = 1, K), \tag{7}$$

where c_p is the mixture specific heat, λ is the mixture thermal conductivity, $\dot{Q}_{\mathrm{rad}}$ is the gas radiation term in the optically-thin limit [24], K is the number of gas-phase species, Y_k, $c_{p,k}$, h_k, $\dot{\omega}_k$, V_k and W_k are the mole fraction, the specific heat, the molar enthalpy, the molar production rate, the multicomponent diffusion velocity, and the molar mass of species k, respectively.

This model has been used to simulate various combustion systems successfully before where the simplified flow reduces computational power required. This is an attractive benefit for cases where coupling with complex and computationally expensive reacting systems is necessary [25, 26].

2.2. Gas phase chemistry

The combustion chemistry and transport data of the gas species were described by the USC-Mech II hydrocarbon kinetic model which includes 111 species and 784 reactions [27]. TTIP was added as an extra species. TTIP thermodynamic data was obtained from first-principle calculations by Buerger et al. [28] while the transport data was estimated from the transport data for large hydrocarbons [29]. The approximation of the transport data was deemed acceptable given the relatively low loading of TTIP simulated in this work. The mechanism, thermodynamic, and transport data used in this study is included in the supplementary material.

2.3. Particle model

2.3.1. Reaction model

In this work, the simple one-step reaction proposed by Okuyama et al. [30] was used to describe the overall rate of TTIP consumption with first order reaction rate constant, k_1, given by

$$k_1 = 3.96 \times 10^5 \exp\left(\frac{-8479.7\ \mathrm{K}}{T}\right)\ \mathrm{s}^{-1}. \tag{8}$$

The overall reaction was assumed to include both gas-phase decomposition and surface reaction of TTIP. The surface reaction rate was described by the first-order rate model proposed by Battiston et al. [31] with rate constant, k_2, derived by Tsantilis et al. [9],

$$k_2 = 1 \times 10^{11} \exp\left(\frac{-15155.16\ \mathrm{K}}{T}\right)\ \mathrm{cm/s}. \tag{9}$$

The rate of the gas-phase decomposition of TTIP was calculated from the difference between the overall and surface reaction rates. When the surface reaction rate exceeds the overall rate, the gas-phase decomposition rate was turned to zero and the surface reaction rate was calculated from the overall rate instead. In summary, the chemical reactions modelled leading to TiO_2 formation are

$$\mathrm{Ti(OC_3H_7)_{4(g)}} \xrightarrow{\mathrm{k}_g} \mathrm{TiO_{2(s)}} + 4\,\mathrm{C_3H_{6(g)}} + 2\,\mathrm{H_2O_{(g)}}$$
$$\mathrm{Ti(OC_3H_7)_{4(g)}} + \mathrm{(TiO_2)_{\mathit{i}-1(s)}} \xrightarrow{\mathrm{k}_s} \mathrm{(TiO_2)_{\mathit{i}(s)}} + 4\,\mathrm{C_3H_{6(g)}} + 2\,\mathrm{H_2O_{(g)}},$$

with the gas-phase reaction rate constant, k_g, and the surface reaction rate constant, k_s, given by

$$k_g = \begin{cases} k_1 - Ak_2 & \text{for } k_1 \geq Ak_2 \\ 0 & \text{for } k_1 < Ak_2 \end{cases} \tag{10}$$

$$k_s = \begin{cases} k_2 & \text{for } k_1 \geq Ak_2 \\ k_1/A & \text{for } k_1 < Ak_2, \end{cases} \tag{11}$$

where A is the total surface area of the particles per unit volume. Considering the relatively low loading of TTIP simulated in this study, these reactions were excluded from temperature source term calculation in Eq. (6).

A similar model was used by Tsantilis et al. [9] and was shown to result in excellent agreement with experimental data. In addition, this reaction rate model was shown to sufficiently describe the overall TTIP consumption in a H_2/O_2 stagnation flame experiment conducted by Korobeinichev et al. [18]. A more recent study of TTIP decomposition in an aerosol reactor [32] also supported the first-order overall rate as proposed by Okuyama et al. [30] for high temperature conditions.

2.3.2. Method of Moments

The particle population was described by the number density moments of the size distribution, M_r, which are defined as

$$M_r = \sum_{i=1}^{\infty} i^r N_i \tag{12}$$

$$\mu_r = \frac{M_r}{M_0}, \tag{13}$$

where r is the order of the moment, N_i is the number density of particles with i TiO_2 monomers, and μ_r are the reduced moments. The method of moments has been widely used to simplify population balance models in areas such as aerosol science, materials science, and cell biology. Hulburt and Katz [33] were one of the first to develop the method of moments to model particles in inhomogeneous flow in 1964. Frenklach and Harris [34] later extended the method to use interpolation to provide closures in the method of moments with interpolative closure (MoMIC), used in this work.

While complete reconstruction of the full particle size distribution requires the knowledge of all moments, a number of relevant properties such as number density, area density, mass density, and average diameter, can be inferred from the first few moments alone. These population properties are given by

$$\text{Number density} = M_0 \tag{14}$$

$$\text{Area density} = A_1 M_{2/3} \tag{15}$$

$$\text{Mass density} = m_1 M_1 \tag{16}$$

$$\text{Average diameter} = d_1 \frac{M_{1/3}}{M_0}, \tag{17}$$

where A_1, m_1 and d_1 are the surface area, the mass, and the diameter of a single TiO_2 monomer, respectively. The surface area and diameter were calculated from m_1 and the bulk density of rutile.

The accuracy of the interpolation used in MoMIC depends on the number of moments. Six moments are normally used, in this case the zeroth to fifth order moments. Thus, the particle population is tracked by only six moment

equations. This provides computational economy without having to make any prior assumptions about the distribution.

The spherical particle model, which assumes instantaneous coalescence, is imposed by the choice of the method of moments model. This assumption is motivated by the fact that the temperature in the combustion zone is much higher than the melting point of bulk TiO_2 (∼1900 K) which leads to rapid sintering. In cases where particles form aggregate structure, a more detailed particle model, which includes aggregation and sintering, is required [35–37].

The particle model was coupled to the flow and gas-phase chemistry through transport equations describing convection, thermal diffusion, size-dependent molecular diffusion and moment source terms. The transport equation for the r^{th}-moment is given in logarithmic form as

$$2U\frac{\mathrm{d}}{\mathrm{d}z}\left(\frac{1}{\rho}\right)+\frac{2U}{\rho}\frac{\mathrm{d}\log M_r}{\mathrm{d}z}+\frac{2}{\rho}\frac{\mathrm{d}U}{\mathrm{d}z}-\frac{2G}{\rho}+\nu_{T,z}\frac{\mathrm{d}\log M_r}{\mathrm{d}z}+\frac{\mathrm{d}\nu_{T,z}}{\mathrm{d}z}- \\ \frac{1}{M_r}\frac{\mathrm{d}}{\mathrm{d}z}\left[\rho D_{p,1}\frac{\mathrm{d}}{\mathrm{d}z}\left(\frac{M_{r-2/3}}{\rho}\right)\right]-\frac{\dot{M}_r}{M_r}=0, \quad (18)$$

where $D_{p,1}$ is the Brownian diffusion coefficient of TiO_2 monomer, $v_{T,z}$ is the thermophoretic velocity, and $\dot{M}_r$ is the moment source terms. The formulations for $D_{p,1}$ and $v_{T,z}$ [38] are given as

$$D_{p,1}=\frac{3}{2\rho}\left(1+\frac{\pi\alpha_T}{8}\right)^{-1}\sqrt{\frac{\bar{W}k_{\mathrm{B}}T}{2\pi N_{\mathrm{A}}}}\left(\frac{1}{d_1^2}\right) \quad (19)$$

$$\nu_{T,z}=-\frac{3}{4}\left(1+\frac{\pi\alpha_T}{8}\right)^{-1}\frac{\mu}{\rho}\frac{\mathrm{d}\log T}{\mathrm{d}z}, \quad (20)$$

where α_T is the thermal accommodation factor which represents the equilibrium fraction of gas molecules that leave the particle surface and is usually about 0.9 [39], $\bar{W}$ is the average molar mass of the gas mixture, k_{B} is the Boltzmann constant, and N_{A} is the Avogadro number.

The moment source terms, $\dot{M}_r$, describe the evolution of the moments according to particle processes, including inception, surface growth, and coagulation,

$$\dot{M}_r=\dot{M}_r^{\mathrm{in}}+\dot{M}_r^{\mathrm{sg}}+\dot{M}_r^{\mathrm{coag}}, \quad (21)$$

where $\dot{M}_r^{\mathrm{in}}$ and $\dot{M}_r^{\mathrm{sg}}$ represent the moment source terms due to inception and surface growth described in the reaction model, respectively. With the reaction model described in Section 2.3.1, these terms are given as

$$\dot{M}_r^{\mathrm{in}}=k_g C_{\mathrm{TTIP}}N_{\mathrm{A}} \qquad \text{for } r\geq 0 \quad (22)$$

$$\dot{M_r^{\mathrm{sg}}}=\begin{cases}0 & \text{for } r=0\\ k_s A_1 C_{\mathrm{TTIP}}N_{\mathrm{A}}\displaystyle\sum_{k=0}^{r-1}\binom{r}{k}\mu_{k+\frac{2}{3}}M_0 & \text{for } r\geq 1,\end{cases} \quad (23)$$

where C_{TTIP} is the TTIP molar concentration in the gas-phase. It is noted that the moment source term due to inception is independent of the moment order, r, because the smallest particle in the population is assumed to have $i = 1$ (i.e. a TiO_2 monomer).

The moment source term due to coagulation, $\dot{M}_r^{\mathrm{coag}}$, follows the formulation proposed by Pratsinis [40],

$$\dot{M}_r^{\mathrm{coag}} = \begin{cases} \dfrac{G_r^c G_r^f}{G_r^c + G_r^f} & \text{for } r \neq 1 \\ 0 & \text{for } r = 1, \end{cases} \tag{24}$$

where G_r^c and G_r^f are the moment source terms due to coagulation in the continuum and free-molecular regimes, respectively. The coagulation source term in the continuum regime for spherical particles is given as [derivation in 41]

$$G_r^c = \begin{cases} -K_c \left(1 + \mu_{\frac{1}{3}}\mu_{-\frac{1}{3}} + K_c'[\mu_{-\frac{1}{3}} + \mu_{\frac{1}{3}}\mu_{-\frac{2}{3}}]\right) M_0^2 & \text{for } r = 0 \\ 0 & \text{for } r = 1 \\ \dfrac{1}{2} K_c \displaystyle\sum_{k=1}^{r-1} \binom{r}{k} \left(\beta_1^c(r,k) + K_c' \beta_2^c(r,k)\right) M_0^2 & \text{for } r \geq 2 \end{cases} \tag{25}$$

$$K_c = \frac{2k_{\mathrm{B}}T}{3\mu} \tag{26}$$

$$K_c' = 2.514\lambda_l \left(\frac{\pi\rho_{\mathrm{TiO_2}}}{6m_1}\right)^{\frac{1}{3}} \tag{27}$$

$$\beta_1^c(r,k) = \mu_{k+\frac{1}{3}}\mu_{r-k-\frac{1}{3}} + 2\mu_k\mu_{r-k} + \mu_{k-\frac{1}{3}}\mu_{r-k+\frac{1}{3}} \tag{28}$$

$$\beta_2^c(r,k) = \mu_{k+\frac{1}{3}}\mu_{r-k-\frac{2}{3}} + \mu_k\mu_{r-k-\frac{1}{3}} + \mu_{k-\frac{1}{3}}\mu_{r-k} + \mu_{k-\frac{2}{3}}\mu_{r-k+\frac{1}{3}}, \tag{29}$$

where λ_l is the mean free path and $\rho_{\mathrm{TiO_2}}$ is the bulk density of rutile titania.

The coagulation source term in the free-moleculer regime for spherical particles is given as [derivation in 41]

$$G_r^f = \begin{cases} -\dfrac{1}{2} K_f \left(\frac{1}{2} f_{0,0}\right) M_0^2 & \text{for } r = 0 \\ 0 & \text{for } r = 1 \\ \dfrac{1}{2} K_f \displaystyle\sum_{k=1}^{r-1} \binom{r}{k} \left(\frac{1}{2} f_{k,r-k}\right) M_0^2 & \text{for } r \geq 2 \end{cases} \tag{30}$$

$$K_f = \epsilon_{i,j} \left(\frac{6k_{\mathrm{B}}T}{\rho_{\mathrm{TiO_2}}}\right)^{\frac{1}{2}} \left(\frac{3m_1}{4\pi\rho_{\mathrm{TiO_2}}}\right)^{\frac{1}{6}} \tag{31}$$

$${}^l f_{x,y} = \sum_{i=1}^{\infty}\sum_{j=1}^{\infty} \frac{i^x j^y}{\sqrt{ij}} (i+j)^l \left(i^{\frac{1}{3}} + j^{\frac{1}{3}}\right)^2 \frac{N_i N_j}{M_0^2}, \tag{32}$$

where $\epsilon_{i,j}$ is the size-dependent collision enhancement factor due to attractive or repulsive inter-particle forces. In this case, a constant multiplier, ϵ, is assumed to replace the size-dependent enhancement factor as normally used for soot coagulation [42]. The enhancement factor used in this study is 2.64 which was calculated by Zhang et al. [43] considering both van der Waals and dipole-dipole interaction of TiO_2 particles in free-molecular regime at high temperature. The enhancement factor used for soot is only slightly lower, 2.2 [42].

Finally, closures for the fractional moment terms were obtained from Lagrange interpolation (or extrapolation in case of negative order moments) among the known values of whole order moments as prescribed by Frenklach et al. [41],

$$\log \mu_p = L_p \left(\log \mu_0, \log \mu_1, ..., \log \mu_{r_{\max}} \right) \qquad \text{for } p > 0 \tag{33}$$

$$\log \mu_p = L_p \left(\log \mu_0, \log \mu_1, \log \mu_2 \right) \qquad \text{for } p < 0. \tag{34}$$

The function ${}^{\frac{1}{2}}f_{x,y}$ was estimated by logarithmic Lagrange interpolation between evaluations of the grid function,

$${}^{m}f_{x,y} = \sum_{k=0}^{m} \binom{m}{k} \left(\mu_{k+x+\frac{1}{6}} \mu_{m+y-k-\frac{1}{2}} + 2\mu_{k+x-\frac{1}{6}} \mu_{m+y-k-\frac{1}{6}} + \mu_{k+x-\frac{1}{2}} \mu_{m+y-k+\frac{1}{6}} \right), \tag{35}$$

for $m \in \mathbb{N}_0$, using the parameterisation

$$m = 0, ..., n-1 \tag{36}$$

$$n = \min(4, U - \max(x, y)) \quad \text{with } U \in \{3, ..., 6\}, \tag{37}$$

where U is the number of moments evolution equations being solved, six in this case, such that $r = 0, ..., U-1$ [44].

2.4. Boundary conditions

The set of governing equations in Eqs. (4)–(7) and (18) represent a fully-coupled system of fluid flow, gas-phase chemistry, and particles. The equations were solved as a boundary value problem by specifying a set of boundary conditions at the burner nozzle and stagnation plane.

The boundary conditions at $z = 0$ (nozzle) are given as

$$U(0) = \frac{\rho_0 u_0}{2} \tag{38}$$

$$G(0) = 0 \tag{39}$$

$$T(0) = T_0 \tag{40}$$

$$\rho(0) Y_k(0) V_k(0) = \rho_0 u_0 (Y_{k,0} - Y_k(0)) \qquad \text{for } k = 1, ..., K \tag{41}$$

$$\log M_r(0) = 0 \qquad \text{for } r = 0, ..., 5, \tag{42}$$

where u_0, ρ_0, T_0, and $Y_{k,0}$ are the exit velocity, density, temperature, and mole fraction of species k of the gas mixture in the nozzle, respectively. The formulation of the boundary condition of the species mole fraction, Y_k, allows for

back-diffusion into the nozzle which leads to $Y_{k,0} \neq Y_k(0)$. As the particles were supposed to be non-existent in the initial gas mixture in the nozzle, M_r should be zero. However, as the moments were tracked in log-space, $\log M_r$, this boundary condition was not feasible. Instead, $\log M_r(0) = 0$ was used, corresponding to negligible but non-zero particle concentration. This choice was justified by the fact that the high temperature region is located far from the nozzle, which results in insensitivity to the choice of $\log M_r(0)$.

The boundary conditions at $z = L$ (stagnation plane) are given as

$$U(L) = 0 \tag{43}$$

$$G(L) = 0 \tag{44}$$

$$T(L) = T_s \tag{45}$$

$$\rho(L) Y_k(L) V_k(L) = 0 \qquad \text{for } k = 1, ..., K \tag{46}$$

$$\frac{\mathrm{d} \log M_r(L)}{\mathrm{d}z} = 0 \qquad \text{for } r = 0, ..., 5, \tag{47}$$

where T_s is the stagnation temperature.

3. Computational details

All of the simulations presented in this work were performed using the *k*inetics® software package [45]. The boundary-value problem, described in Section 2.4, was solved using a damped Newton search algorithm to obtain the steady-state solution [similar to 46].

The convergence criterion was specified by setting a tolerance level which controls the grid refinement to resolve the regions with large magnitudes of the gradient and curvature of the dependent variables. Using the solution-adapted grid refinement, convergence was achieved with 250–300 grid points for the nozzle-stagnation plate separation distance, $H = 1.27$ cm, and 400–450 grid points for $H = 3.4$ cm. By way of comparison, Modak et al. [22] used only around 200 grid points for $H = 3.4$ cm with a similar flame.

The experimental conditions in Tolmachoff et al. [14] were used in all simulations in this work except where otherwise stated. The initial molar composition of the gas mixture was 3.96% C_2H_4, 26.53% O_2, and 69.51% Ar (corresponding to an equivalence ratio of $\phi = 0.45$) while TTIP loading was varied from 10–2000 ppm. The other boundary conditions were specified as

$$u_0 = 429 \text{ cm/s}$$
$$T_0 = 423.15 \text{ K}$$
$$T_s = 400 - 1600 \text{ K}.$$

The gas radiation model for temperature correction, under the assumption of optically-thin flames, including the radiation from H_2O, CO_2, CO, and CH_4 [47], was used for all simulations presented in this work.

4. Results and discussion

4.1. Flame location

In the experimental study by Tolmachoff et al. [14], the distance between the stagnation surface and the nozzle, L, is 3.4 cm and the nozzle exit diameter, d, is 1 cm. This high L/d ratio is an important parameter to consider because ideal one-dimensional stagnation flow equations assume an infinitely wide nozzle exit diameter ($L/d \approx 0$). As a result of the high L/d ratio, a free-jet region with plug flow velocity profile is formed upstream of the flame. This free-jet region is not captured by the parabolic solution of the one-dimensional stagnation flow model [48, 49].

The best solution to this problem is to specify boundary conditions downstream of the free-jet region where the flow can be modelled as a one-dimensional stagnation flow [48]. However, this would require knowledge of the full velocity profile which could only be determined experimentally or with rigorous fluid dynamics simulation.

An alternative solution is to fit the predicted temperature profile to the experimental measurement [14, 18]. This is done by specifying a computational distance, H, that excludes the free-jet region such that $H < L$. In other words, the one-dimensional stagnation flow behaviour is assumed to start at the end of the free-jet region. Nevertheless, this approach requires an accurate temperature profile which is not available due to the large uncertainty in the reported temperature measurement [14].

In this work, information about the flame location is used to determine the computational distance, H. It is assumed that OH*-chemiluminescence is responsible for the experimentally observed luminosity of the flame. This is a reasonable assumption given that the non-sooting, lean flame is used where particle radiation could be neglected. The peak luminosity is observed at 0.29 ± 0.03 cm from the substrate [14]. The distance $H = 1.27$ cm is chosen such that the location of the OH* peak predicted by the model coincides with the experimentally observed peak luminosity (this is illustrated in Fig. 2).

Without taking into account the existence of the free-jet region, the calculation of one-dimensional stagnation flame with $H = 3.4$ cm, not shown here for brevity, would result in the flame located almost 1 cm away from the stagnation surface. This is significantly different from the experimental observation and leads to a much longer particle residence time in the combustion zone. The maximum temperature is also higher due to less heat loss to the stagnation plate.

4.2. Flame structure

Figure 3 shows the steady-state solution for an undoped flame. The results are plotted with $z = 0$ being the location of the nozzle (as for all figures in this work). The stagnation surface is located at $z = 3.378$ cm, instead of 3.4 cm, in order to allow comparison with measurement and calculation done by Tolmachoff et al. [14].

Figure 3(a) shows the simulated temperature profile for an undoped flame as well as the experimental measurement and calculation reported by Tolmachoff et al. While Tolmachoff et al. do not explicitly state whether the measurement was conducted with a doped or undoped flame, given that direct comparison is made with undoped flame simulations in their work, we assume here that the measurement is performed for an undoped flame. This is consistent with the current work as the simulated maximum temperature ($T_{\max} = 2123.8$ K) shows an excellent agreement with the experiment ($T_{\max} = 2124 \pm 50$ K). The simulated temperature profile also shows an acceptable agreement given the spatial uncertainty of the measurement.

A similar trend is shown for both experimental and simulated temperature profiles. Initially, the temperature is constant, equal to the gas temperature in the nozzle. At $z \sim 3.0$ cm the temperature starts to increase sharply, reaching a maximum temperature at $z \sim 3.25$ cm. This high temperature region is subsequently referred to as the combustion zone. The width of the combustion zone is predicted to be slightly less than 0.4 cm which is consistent with experimental observation. Near the stagnation surface, there is a rapid decrease in the temperature as a result of heat loss to the plate.

In a doped flame, decomposition of TTIP releases gaseous fuel propene, C_3H_6. This results in increasing maximum temperature with increasing TTIP loading (around 120 K difference between 0 and 1070 ppm). The effect of TTIP loading is discussed further in Section 4.5.1.

The axial velocity calculated in Fig. 3(a) is the total of convective and thermophoretic velocities. The axial velocity initially decreases to 113 cm/s at $z = 3.0$ cm due to flow divergence. At the edge of the combustion zone, the axial velocity increases sharply as a result of strong gas expansion. It is noted that at the stagnation surface, the axial velocity is not zero (≈ 23 cm/s), corresponding to the thermophoretic velocity. The velocity profile calculation by Tolmachoff et al. only considers convective velocity and thus a zero velocity is shown at the stagnation surface.

Overall, the leading edge of combustion zone calculated by Tolmachoff et al. appears shifted ~ 0.5 cm closer to the stagnation surface as compared to the current work. This suggests that a computational distance, $H < 1.27$ cm is employed although no exact value is reported. Presumably, the peak of H atom concentration is used by Tolmachoff et al. to determine the flame location, in contrast to the assumption used in this work (see Section 4.1).

The calculated major species profiles are shown in Fig. 3(b). Similar shift towards the stagnation surface is observed for calculation by Tolmachoff et al. Both H and OH profiles start to increase sharply at $z = 3.0$ cm, where the temperature increases rapidly. It is noted that H mole fraction reaches a maximum slightly before OH mole fraction, explaining the difference in computational distance employed by Tolmachoff et al.

4.3. Particle moments and TTIP profiles

Figure 4 shows the evolution of particle size moments in the combustion zone. Before the combustion zone, the moments are virtually constant showing

little to no particle processes occuring. The sharp increase in all particle moments, M_0–M_5, shows the formation of particles inside the combustion zone. Initially, all moments are similar in magnitude which indicates nucleation of TiO_2 monomers. As the surface growth and coagulation rates increase, the higher order moments increase more sharply compared to the lower order moments. Near the stagnation surface, the higher order moments increase while the zeroth order moment, M_0, decreases slightly. This is a characteristic of coagulation.

Similar to the particle moments, Fig. 4 shows that the TTIP mole fraction is constant before the combustion zone. The TTIP mole fraction decreases in the combustion zone as it is consumed by inception and surface growth. Close to the stagnation surface ($z > 3.3$ cm), the TTIP mole fraction approaches zero, showing that TTIP is almost completely converted to TiO_2 in this region. This is expected considering the high temperature in the combustion zone.

4.4. Particle size and GSD

Tolmachoff et al. [14] shows that the particle size distributions follow a log-normal distribution for all TTIP loadings considered. The fitted particle size distribution is described by its median particle size, $\langle D_p \rangle$, and geometric standard deviation, GSD. In the current work, the parameters $\langle D_p \rangle$ and GSD were calculated using the following relations [50],

$$\langle D_p \rangle = \frac{D_p}{\sqrt{1 + \frac{\sigma^2}{D_p^2}}} \tag{48}$$

$$\mathrm{GSD} = \exp \sqrt{\log \left(1 + \frac{\sigma^2}{D_p^2} \right)}, \tag{49}$$

where D_p and σ are the mean and the standard deviation of the particle size distribution calculated from the reduced particle moments (derivation in Appendix A), respectively,

$$D_p = d_1 \mu_{\frac{1}{3}} \tag{50}$$

$$\sigma = d_1 \sqrt{\mu_{\frac{2}{3}} - \mu_{\frac{1}{3}}^2}. \tag{51}$$

Before comparing the model prediction to the experimental data, it is important to consider two aspects of the experimental work performed by Tolmachoff et al. [14] which affect the particle size measurement, namely stagnation plate rotation and stagnation temperature.

The particle size measurement is reported for stationary and rotating stagnation plate, employing different particle sampling techniques. A scanning mobility particle sizer (SMPS) is used to measure the particle mobility diameter in stationary stagnation plate cases with the sampling probe mounted inside the plate. On the other hand, transmission electron microscopy (TEM) analysis with rapid insertion probe is used to measure the primary particle diameter in the rotating stagnation plate cases.

The rotation, combined with four equally spaced cold jets placed at the back of the stagnation plate, results in cooling of the stagnation surface. With a total cooling jet volumetric flow of 40 L/min, the stagnation plate temperature, T_s, is shown to be stabilized at $\sim$ 400 K for rotational speed in the range 100–600 rpm. Without rotation (i.e. 0 rpm), the absence of convective cooling leads to T_s reaching as high as $\sim$1000 K although exact measurement is not reported.

Stationary cases

Taking into account the lack of convective cooling, the temperature of the stationary stagnation surface is assumed to be 1000 K. The simulated particle median size at the stagnation surface ($\delta = 0$) with $T_s = 1000$ K, presented in Fig. 5(a), shows a good agreement with the experimental data. For ease of comparison, the simulated and experimental $\langle D_p \rangle$ and GSD for the five TTIP loadings tested are also presented in Table 1. In general, particle size is predicted to increase as a function of TTIP loading.

Similar trend is also observed for particle GSD in Fig. 5(b), both in the model prediction and experiment. It is noted that for high TTIP loading, the model underpredicts the particle GSD. This underprediction appears significant due to the narrow particle size distributions where GSD is extremely sensitive to distribution width. This is illustrated in Fig. 6, where the log normal density functions for measured and simulated distribution for $T_s = 1000$ K are compared. It shows a relatively insignificant difference in the distribution width given the difference in GSD.

Rotating cases

Tolmachoff et al. show that there is a substantial decrease in primary particle size measured with TEM analysis for the rotating cases compared to the mobility particle size measured with SMPS for stationary case. For instance, in a 1070 ppm TTIP flame, TEM analysis gives median primary particle diameter of 8.5–9.8 nm for 100–600 RPM rotation while SMPS measurement gives median mobility particle diameter of 13 nm. This comparison, however, can only be made under the assumption of complete coalescence of particles, i.e. primary particle diameter is equal to mobility diameter.

Assuming that complete coalescence occurs, Tolmachoff et al. suggest that the difference can be explained by the difference in stagnation surface temperature in rotating and stationary plate cases. Figure 5 shows the predicted median particle size and GSD for surface temperature of 400 K. It is shown that there is indeed some decrease in particle size as the surface temperature decreases but it does not seem to be enough to explain the significant discrepancy in the measured particle size.

It is possible that the decrease in measured particle size is a consequence of significant level of aggregation in the flame. Compared to stationary stagnation cases, the gas temperature near the plate for the rotating cases is expected to be significantly lower, shown in Fig. 8(b). This results in slower particle sintering

relative to coagulation, leading to formation of aggregate structure. In this case, a more detailed particle model is required to fully capture the effects of aggregation. The presence of aggregation, however, is not directly confirmed in the experiment. Thus, the extent of aggregation and its implications on the interpretation of the experimental data remains a question to be investigated in the future work.

Some other factors could also affect the interpretation of experimental data for rotating stagnation surface. For example, the effects of rotating plate on stagnation flow and boundary layer thickness. At this stage, the extent of these effects remain as open questions.

4.5. Effects of process parameters

4.5.1. Precursor loading

Figure 7(a) shows the simulated temperature profiles as a function of the TTIP loading. Increasing TTIP loading from 10 to 1070 ppm increases $T_{\max}$ from 2130 K to 2240 K due to the release of C_3H_6. Thus, a slight increase in the thermophoretic velocity near the stagnation surface is expected. The combustion zone and OH* profile are slightly broadened, which results in small shifts in the initial temperature increase and OH* peak locations. The shift in the OH* peak location is from 3.10 to 3.13 cm.

Figure 7(b) shows the mean particle size, D_p, and particle number concentration, n_p. The number concentration, n_p, is normalized by the gas density, ρ_{gas}, to remove the effect of volume expansion. Initially, n_p increases sharply due to inception of TiO_2 monomers, especially for high TTIP loading. This is followed by a gradual decrease for high TTIP loading while almost constant n_p for low TTIP loading. For all cases, D_p increases most sharply at the upstream edge of the combustion zone, at $z \sim 3$ cm, and also near the stagnation surface.

It is noted that the initial growth region in Fig. 7(b) starts at around 0.4 cm from stagnation surface, earlier than that claimed by Tolmachoff et al. [14]. Tolmachoff et al. assume that after the temperature reached 1850 K (at ~ 0.3 cm from stagnation surface), TTIP undergoes rapid decomposition into Ti atoms which are oxidized and then nucleate. This is in contrast with the kinetically-limited decomposition model employed in this work (Section 2.3.1) and other studies [9, 21]. As a consequence of using this reaction model, the simulated nucleation and surface growth coincide with the onset of initial temperature increase at the leading edge of the flame (Fig. 7(a), ~ 0.4 cm from the stagnation surface). In addition, the difference in modelling assumption used to determine the computational distance (see Section 4.1) results in a slight shift of the flame edge in this work compared to calculation by Tolmachoff et al.

Figure 7(c) compares the coagulation and surface growth rates in the combustion zone. Similar to n_p, the rates are also normalized with ρ_{gas}. Note that the coagulation rate has the opposite sign to $\mathrm{d}M_0/\mathrm{d}t$ because M_0 decreases with coagulation. As temperature increases rapidly in the combustion zone, both surface growth and coagulation rates increase sharply (note the log-scale) because of the high concentration of TiO_2 monomers. As expected, the rates

increase with increasing TTIP loading. In this region, the surface growth rate is a few order of magnitude higher than the coagulation rate. This indicates that surface growth is important in the initial stage of particle growth.

As the particles flow downstream ($z = 3.05 - 3.35$ cm), the coagulation and surface growth rates decrease due to the consumption of TiO_2 monomers and TTIP, respectively. This is also shown by the steady decrease of n_p and slower increase in D_p in Fig. 7(b).

Near the stagnation surface ($z > 3.35$ cm), both surface growth and coagulation rates start to decrease more sharply due to the steep decrease in temperature. The surface growth rate decreases much faster than the coagulation rate (surface growth rate drops from 10^{20} to 10^{10} while coagulation rate drops from 10^{17} to 10^{16} /s.g of gas for 1070 ppm loading). Therefore, coagulation becomes more dominant compared to surface growth in this region. This could explain the apparent faster increase in D_p and decrease in n_p for higher TTIP loading.

The coagulation-dominated growth at this region leads to sensitivity of particle size to the sampling location near the stagnation surface, which increases with increasing TTIP loading.

4.5.2. Stagnation temperature, T_s

In order to evaluate the effect of the stagnation temperature, the cases with $T_s = 400$, 1000, and 1600 K are simulated for 1070 ppm TTIP loading. The results are shown in Fig. 8.

Figure 8(a) shows that increasing T_s broadens the temperature and OH* profiles and significantly reduces the temperature gradient near the stagnation surface. $T_{\max}$ increases slightly (2241 K for $T_s = 400$ K, 2260 K for $T_s = 1600$ K) due to less heat loss to the plate. The location of OH* peak shifts slightly from $z = 3.12$ to 3.13 cm (for $T = 400$ and 1600 K, respectively).

As described previously, nucleation initially dominates at the start of the combustion zone, followed by surface growth and coagulation. Figure 8(b) shows a slight shift in the start of the combustion zone. This leads to an earlier increase (and subsequent decrease) of n_p for higher T_s. Thus, at $z \sim 3.3$ cm, n_p is lowest for $T_s = 1600$ K (also for coagulation rate in Fig. 8(c)).

Near the stagnation surface ($z > 3.3$ cm), there is a sharper increase in D_p for higher T_s despite the lower coagulation rate, as shown in Fig. 8(c). This is explained by examining the particle time history near the stagnation surface, calculated from the total of convective and thermophoretic velocities. Higher T_s leads to smaller thermophoretic velocity and consequently, longer residence time near the stagnation surface. As a result, the spatial sensitivity of the particle size is expected to be larger for higher T_s. A similar trend is also observed for smaller TTIP loading.

4.6. Role of surface growth

So far, it has been demonstrated that coagulation plays an important role in the post flame region near the stagnation surface. In this section, the role of surface growth is evaluated by comparing the reaction model described in Section 2.3.1 with a reaction model that assumes no surface growth [22]. Without

surface growth, the nucleation rate is equal to the overall TTIP decomposition rate. The gas-phase composition and temperature profile are identical in both models because of the equal rate of C_3H_6 release, which is governed by the overall reaction rate.

Figure 9(a) presents the particle size evolution along the flame for both models (with 96 ppm TTIP loading, $T_s = 400$ K). It shows that without surface growth, the particle size is significantly smaller at all locations in the combustion zone. The most important difference is in the initial growth region at the upstream edge of the combustion zone, which shows a more gradual increase of D_p without surface growth compared to the steep increase of D_p with surface growth. This highlights the important role of the surface reaction in the initial growth stage.

Eventually, the slower growth of the particles at the upstream edge of combustion zone leads to an underprediction of the particle size at the stagnation surface ($z = 3.4$). Figure 9(b) shows the sampled particle size at $z = 3.4$ with and without surface growth for different TTIP loading, showing similar trend for all loadings considered in this work.

Figure 9(c) shows the calculated GSD profiles for all cases considered by assuming a log-normal distribution. However, in the initial growth region ($z \sim 2.4$ cm for $H = 3.4$ cm and $z \sim 3$ cm for $H = 1.27$ cm) the particle distribution is not expected to follow a log-normal distribution. This results in an unexpected behaviour as shown by peaks and oscillations in the inception region. For the model with surface growth, further growth of particles after inception region proceeds mainly through surface growth, which explains the slower increase in particle GSD. In contrast, for the model with no surface growth, the particles grow through only coagulation, resulting in rapid increase in particle GSD (widening of particle distribution). Eventually, the GSD decreases to approach the GSD of a self-preserving size distribution [17]. The calculated GSDs at the stagnation surface indicate significantly broader particle size distribution functions, PSDFs, (with GSD > 1.5) when surface growth is neglected. This is inconsistent with the experimental observation [14].

The original simulations using the model without surface growth [22] appears to yield a good agreement with experimental data. However, the simulations were performed without correcting the computational distance related to the free-jet region. As discussed earlier in Section 4.1, simulation with $H = 3.4$ cm leads to significantly wider combustion zone. As a result, the slower particle growth is compensated by the longer particle residence time.

It is noted that the importance of surface reaction in the initial particle growth stage has been predicted in the study by Tsantilis et al. [9] (for a premixed flat burner). However, particle sampling close to the flat burner face (< 0.5 cm), where particles are newly incepted, was not feasible. In contrast, a stagnation burner configuration allows experimental investigation of the initial particle growth stage where the masking effect of coagulation is minimized. This results in a high sensitivity to surface growth. Hence, the FSRS setup is a good candidate to investigate TTIP decomposition kinetics and test more detailed TTIP decomposition models.

5. Conclusions

A spherical particle model describing TiO_2 formation in a stagnation flame reactor is developed by assuming a simple one-step TTIP decomposition reaction and complete coalescence. In order to compare the simulation results with experimental data, it is important to account for the existence of the free-jet region in the flow. In this work, this is done by matching the location of the simulated OH* peak with the experimentally observed flame location. The computational distance used in this work is 1.27 cm.

In general agreement with the experimental observation, the simulated average particle size and standard deviation increase with increasing TTIP loading and stagnation temperature. The model successfully reproduced the average particle sizes measured with a stationary stagnation surface, with $L = 3.4$ cm, as functions of TTIP loading although some discrepancy in particle GSD is observed. If complete coalescence and negligible effect of rotation on the flow are assumed, the simulated particle size with $T = 400$ K significantly overpredicts the particle size obtained from rotating surface experiment. This suggests the presence of significant aggregation in rotating surface cases or effect of surface rotation on the flow not captured in this model.

Coagulation is shown to be a dominant process near the stagnation surface. This leads to a high spatial sensitivity of the particle size to the sampling location near the stagnation surface for high TTIP loading. The sensitivity increases with increasing stagnation temperature because of the longer particle residence time near the stagnation surface.

Further, surface growth is found to play an important role during the initial particle growth at the leading edge of the flame. With decreasing length of combustion zone, surface growth becomes increasingly more important than coagulation in overall. This leads to formation of particles with narrow size distribution and high sensitivity to surface growth. These characteristics make the stagnation flame reactor an attractive experimental tool to validate and improve on the scarce kinetic data available in literature on TTIP decomposition.

6. Acknowledgements

This project is supported by the National Research Foundation (NRF), Prime Minister's Office, Singapore under its Campus for Research Excellence and Technological Enterprise (CREATE) programme. The authors also thank CMCL Innovations for generous financial support.

Appendix A. Derivation of D_p and σ

The mean of a particle size distribution, D_p, is given by

$$D_p = \frac{1}{\sum N_i} \sum_i d_i N_i, \tag{A.1}$$

where d_i is the diameter of particle with size i. Assuming a spherical particle where $d_i = i^{\frac{1}{3}} d_1$,

$$D_p = \frac{1}{\sum N_i} \sum_i i^{\frac{1}{3}} N_i d_1 \tag{A.2}$$

$$D_p = \frac{M_{\frac{1}{3}}}{M_0} d_1 = \mu_{\frac{1}{3}} d_1. \tag{A.3}$$

The standard deviation, σ, is given by

$$\sigma = \left(\frac{1}{\sum N_i} \sum_i N_i (d_i - D_p)^2 \right)^{1/2} \tag{A.4}$$

$$\sigma = \left(\frac{1}{M_0} \sum_{i=1}^{\infty} N_i \left(i^{\frac{1}{3}} - \mu_{\frac{1}{3}} \right)^2 {d_1}^2 \right)^{1/2} \tag{A.5}$$

$$\sigma = \left(\frac{1}{M_0} \sum_{i=1}^{\infty} N_i \left(i^{\frac{2}{3}} - 2 i^{\frac{1}{3}} \mu_{\frac{1}{3}} + {\mu_{\frac{1}{3}}}^2 \right) \right)^{1/2} d_1 \tag{A.6}$$

$$\sigma = \sqrt{\mu_{\frac{2}{3}} - {\mu_{\frac{1}{3}}}^2} d_1. \tag{A.7}$$

References

[1] U.S. Geological Survey, Mineral commodity summaries 2016: U.S. Geological Survey, 2016. doi:10.3133/70140094.

[2] M. Kraft, Modelling of particulate processes, KONA Powder Part. J. 23 (2005) 18–35.

[3] R. H. West, G. J. O. Beran, W. H. Green, M. Kraft, First-principles thermochemistry for the production of TiO_2 from $TiCl_4$, J. Phys. Chem. A 111 (2007) 3560–3565.

[4] R. H. West, R. A. Shirley, M. Kraft, C. F. Goldsmith, W. H. Green, A detailed kinetic model for combustion synthesis of titania from $TiCl_4$, Combust. Flame 156 (2009) 1764–1770.

[5] R. Shirley, Y. Liu, T. S. Totton, R. H. West, M. Kraft, First-principles thermochemistry for the combustion of a $TiCl_4$ and $AlCl_3$ mixture, J. Phys. Chem. A 113 (2009) 13790–13796.

[6] R. Shirley, J. Akroyd, L. A. Miller, O. R. Inderwildi, U. Riedel, M. Kraft, Theoretical insights into the surface growth of rutile TiO_2, Combust. Flame 158 (2011) 1868–1876.

[7] R. Shirley, W. Phadungsukanan, M. Kraft, J. Downing, N. E. Day, P. Murray-Rust, First-principles thermochemistry for gas phase species in an industrial rutile chlorinator, J. Phys. Chem. A 114 (2010) 11825–11832.

[8] T. S. Totton, R. Shirley, M. Kraft, First-principles thermochemistry for the combustion of $TiCl_4$ in a methane flame, Proc. Combust. Inst. 33 (2011) 493–500.

[9] S. Tsantilis, H. K. Kammler, S. E. Pratsinis, Population balance modeling of flame synthesis of titania nanoparticles, Chem. Eng. Sci. 57 (2002) 2139–2156.

[10] S. Tsantilis, S. E. Pratsinis, Narrowing the size distribution of aerosol-made titania by surface growth and coagulation, J. Aerosol Sci. 35 (2004) 405–420.

[11] H. Zhao, X. Liu, S. D. Tse, Effects of pressure and precursor loading in the flame synthesis of titania nanoparticles, J. Aerosol Sci. 40 (2009) 919–937.

[12] M. Yu, J. Lin, T. Chan, Numerical simulation of nanoparticle synthesis in diffusion flame reactor, Powder Technol. 181 (2008) 9–20.

[13] K. Wegner, S. E. Pratsinis, Nozzle-quenching process for controlled flame synthesis of titania nanoparticles, AIChE J. 49 (2003) 1667–1675.

[14] E. D. Tolmachoff, A. D. Abid, D. J. Phares, C. S. Campbell, H. Wang, Synthesis of nano-phase TiO_2 crystalline films over premixed stagnation flames, Proc. Combust. Inst. 32 (2009) 1839–1845.

[15] S. Nikraz, H. Wang, Dye sensitized solar cells prepared by flames stabilized on a rotating surface, Proc. Combust. Inst. 34 (2013) 2171–2178.

[16] S. Memarzadeh, E. D. Tolmachoff, D. J. Phares, H. Wang, Properties of nanocrystalline TiO_2 synthesized in premixed flames stabilized on a rotating surface, Proc. Combust. Inst. 33 (2011) 1917–1924.

[17] F. S. Lai, S. K. Friedlander, J. Pich, G. M. Hidy, The self-preserving particle size distribution for Brownian coagulation in the free-molecule regime, J. Colloid Interface Sci. 39 (1972) 395–405.

[18] O. P. Korobeinichev, A. G. Shmakov, R. A. Maksyutov, A. G. Tereshchenko, D. A. Knyazkov, T. A. Bolshova, M. L. Kosinova, V. S. Sulyaeva, J. S. Wu, Synthesis of mesoporous nanocrystalline TiO_2 films in a premixed $H_2/O_2/Ar$ flame, Combust. Explos. Shock Waves 48 (2012) 49–56.

[19] E. D. Tolmachoff, S. Memarzadeh, H. Wang, Nanoporous titania gas sensing films prepared in a premixed stagnation flame, J. Phys. Chem. C 115 (2011) 21620–21628.

[20] P. Buerger, D. Nurkowski, J. Akroyd, M. Kraft, A kinetic mechanism for the thermal decomposition of titanium tetraisopropoxide, Proc. Combust. Inst. (2016).

[21] A. G. Shmakov, O. P. Korobeinichev, D. A. Knyazkov, A. A. Paletsky, R. A. Maksutov, I. E. Gerasimov, T. A. Bolshova, V. G. Kiselev, N. P. Gritsan, Combustion chemistry of $Ti(OC_3H_7)_4$ in premixed flat burner-stabilized $H_2/O_2/Ar$ flame at 1 atm, Proc. Combust. Inst. 34 (2013) 1143–1149.

[22] A. Modak, K. Puduppakkam, C. Naik, E. Meeks, Simulation of particle synthesis by premixed laminar stagnation flames, Mater. Res. Soc. Symp. Proc. 1506 (2013).

[23] R. J. Kee, J. A. Miller, G. H. Evans, G. Dixon-Lewis, A computational model of the structure and extinction of strained, opposed flow, premixed methane-air flames, Symp. (Int.) Combust. 22 (1989) 1479–1494.

[24] R. Siegel, Thermal radiation heat transfer, fourth edition, Taylor & Francis, 2001.

[25] E. K. Y. Yapp, D. Chen, J. Akroyd, S. Mosbach, M. Kraft, J. Camacho, H. Wang, Numerical simulation and parametric sensitivity study of particle size distributions in a burner-stabilised stagnation flame, Combust. Flame 162 (2015) 2569–2581.

[26] J. Camacho, C. Liu, C. Gu, H. Lin, Z. Huang, Q. Tang, X. You, C. Saggese, Y. Li, H. Jung, L. Deng, I. Wlokas, H. Wang, Mobility size and mass of nascent soot particles in a benchmark premixed ethylene flame, Combust. Flame 162 (2015) 3810–3822.

[27] H. Wang, X. You, A. V. Joshi, S. G. Davis, A. Laskin, F. Egolfopoulos, C. K. Law, USC mech version II. High-temperature combustion reaction model of H_2/CO/C_1-C_4 compounds, 2007. URL: `http://ignis.usc.edu/USC_Mech_II.htm`, accessed on 12 December 2015.

[28] P. Buerger, D. Nurkowski, J. Akroyd, S. Mosbach, M. Kraft, First-principles thermochemistry for the thermal decomposition of titanium tetraisopropoxide, J. Phys. Chem. A 119 (2015) 8376–8387.

[29] Chemical-kinetic mechanisms for combustion applications, San Diego mechanism web page, Mechanical and Aerospace Engineering (combustion research), University of California at San Diego, 2012. URL: `http://combustion.ucsd.edu`, accessed on 4 January 2016.

[30] K. Okuyama, R. Ushio, Y. Kousaka, R. C. Flagan, J. H. Seinfeld, Particle generation in a chemical vapor deposition process with seed particles, AIChE J. 36 (1990) 409–419.

[31] G. A. Battiston, R. Gerbasi, M. Porchia, A. Gasparotto, Metal organic CVD of nanostructured composite TiO_2-Pt thin films : A kinetic approach, Chem. Vap. Deposition 5 (1999) 13–20.

[32] Y. Wang, P. Liu, J. Fang, W.-N. Wang, P. Biswas, Kinetics of sub-2 nm TiO_2 particle formation in an aerosol reactor during thermal decomposition of titanium tetraisopropoxide, J. Nanopart. Res. 17 (2015) 147.

[33] H. M. Hulburt, S. Katz, Some problems in particle technology, Chem. Eng. Sci. 19 (1964) 555–574.

[34] M. Frenklach, S. J. Harris, Aerosol dynamics modeling using the method of moments, J. Colloid Interface Sci. 118 (1987) 252–261.

[35] W. J. Menz, M. Kraft, The suitability of particle models in capturing aggregate structure and polydispersity, Aerosol Sci. Technol. 47 (2013) 734–745.

[36] N. M. Morgan, R. I. A. Patterson, M. Kraft, Modes of neck growth in nanoparticle aggregates, Combust. Flame 152 (2008) 272–275.

[37] D. Grosschmidt, H. Bockhorn, M. Goodson, M. Kraft, Two approaches to the simulation of silica particle synthesis, Proc. Combust. Inst. 29 (2002) 1039–1046.

[38] L. Waldmann, K. H. Schmitt, Thermophoresis and diffusiophoresis of aerosols, Academic Press New York, 1966.

[39] S. Friedlander, Smoke, dust, and haze: Fundamentals of aerosol behavior, Topicals in chemical engineering, Wiley, 1977.

[40] S. E. Pratsinis, Simultaneous nucleation condensation and coagulation in aerosol reactors, J. Colloid Interface Sci. 124 (1988) 416–427.

[41] M. Frenklach, Method of moments with interpolative closure, Chem. Eng. Sci. 57 (2002) 2229–2239.

[42] S. J. Harris, I. M. Kennedy, The coagulation of soot particles with van der Waals forces, Combust. Sci. Technol. 59 (1988) 443–454.

[43] Y. Zhang, S. Li, W. Yan, Q. Yao, S. D. Tse, Role of dipole-dipole interaction on enhancing Brownian coagulation of charge-neutral nanoparticles in the free molecular regime, J. Chem. Phys. 134 (2011) 10755–10760.

[44] J. Akroyd, A. J. Smith, R. A. Shirley, L. R. McGlashan, M. Kraft, A coupled CFD-population balance approach for nanoparticle synthesis in turbulent reacting flows, Chem. Eng. Sci. 66 (2011) 3792–3805.

[45] CMCL Innovations, *k*inetics®, 2016. URL: `http://www.cmclinnovations.com/`.

[46] J. F. Grcar, The Twopnt program for boundary value problems, Technical Report SAND91-8230, Sandia National Laboratories, 1992.

[47] R. S. Barlow, A. N. Karpetis, J. H. Frank, J. Y. Chen, Scalar profiles and NO formation in laminar opposed-flow partially premixed methane/air flames, Combust. Flame 127 (2001) 2102–2118.

[48] J. M. Bergthorson, K. Sone, T. W. Mattner, P. E. Dimotakis, D. G. Goodwin, D. I. Meiron, Impinging laminar jets at moderate Reynolds numbers and separation distances, Phys. Rev. E 72 (2005) 066307.

[49] J. M. Bergthorson, S. D. Salusbury, P. E. Dimotakis, Experiments and modelling of premixed laminar stagnation flame hydrodynamics, J. Fluid Mech. 681 (2011) 340–369.

[50] A. M. Mood, F. A. Graybill, D. C. Boes, Introduction to the theory of statistics, 3rd ed., New York: McGraw-Hill, 1974.

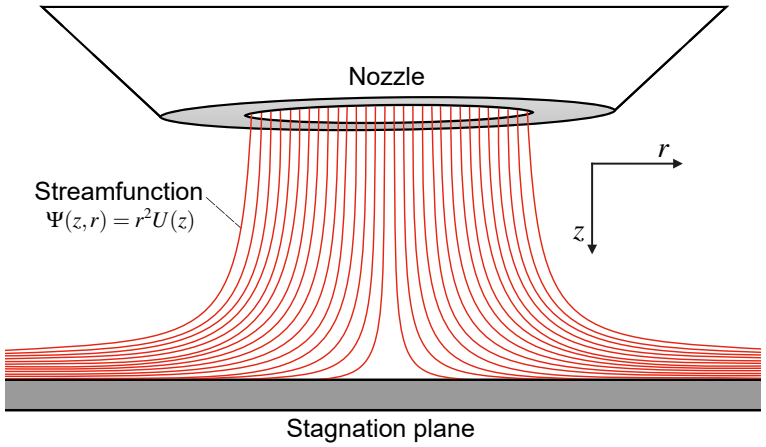

Figure 1: Diagram of a one-dimensional stagnation flow with streamlines shown in red.

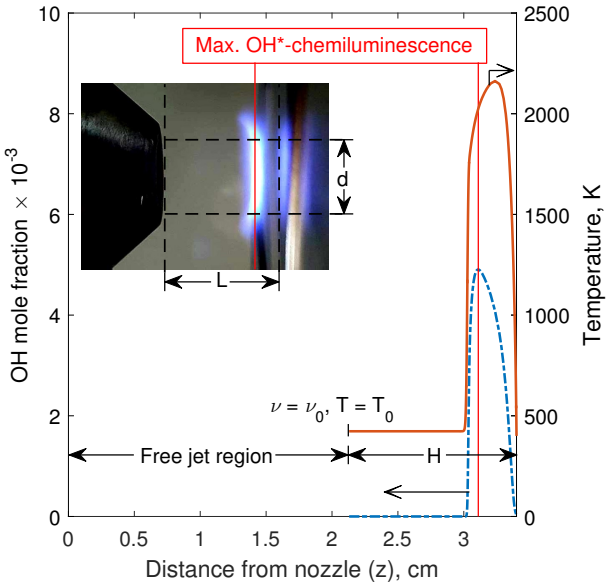

Figure 2: Simulated temperature and OH*-mole fraction profiles showing the free-jet region upstream of the flame (306 ppm TTIP, $H = 1.27$ cm, $T_s = 400$ K). The inset illustrates the experimental setup and does not correspond to any specific simulation presented in the figure. It shows a flat undoped flame stabilized near the stagnation surface rotating at 300 rpm. The vertical solid lines indicate the location of max. OH*-chemiluminescence.

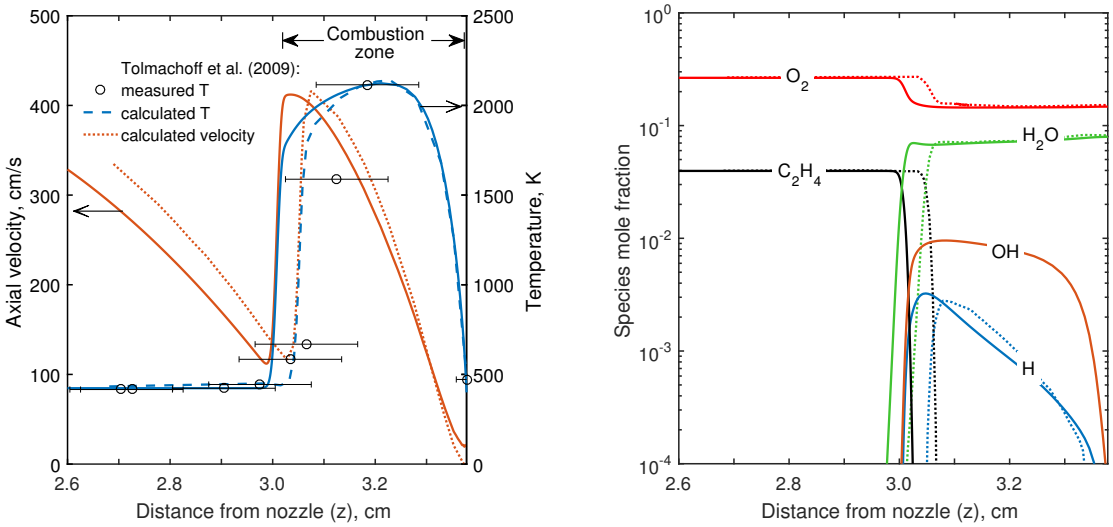

(a) Temperature and axial velocity profiles.

(b) Major species mole fractions.

Figure 3: Calculated undoped flame structure with $H = 1.27$ cm and $T_s = 400$ K in this work (solid lines). The temperature measurement (symbol) and calculated flame structure from [14] are included (broken lines).

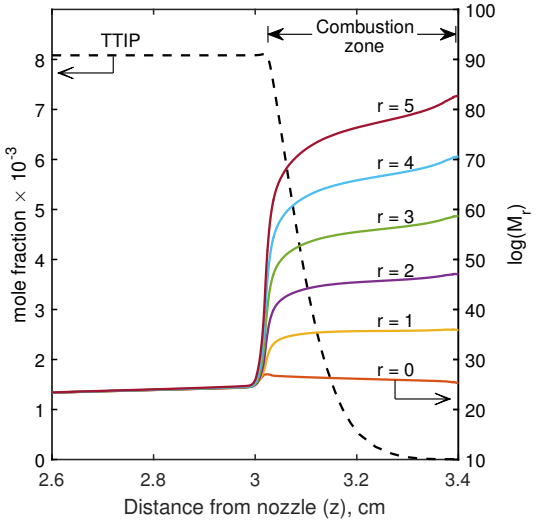

Figure 4: Simulated particle moments, M_r, evolution (r = moments order) and TTIP mole fraction profiles for 1070 ppm TTIP loading ($H = 1.27$ cm).

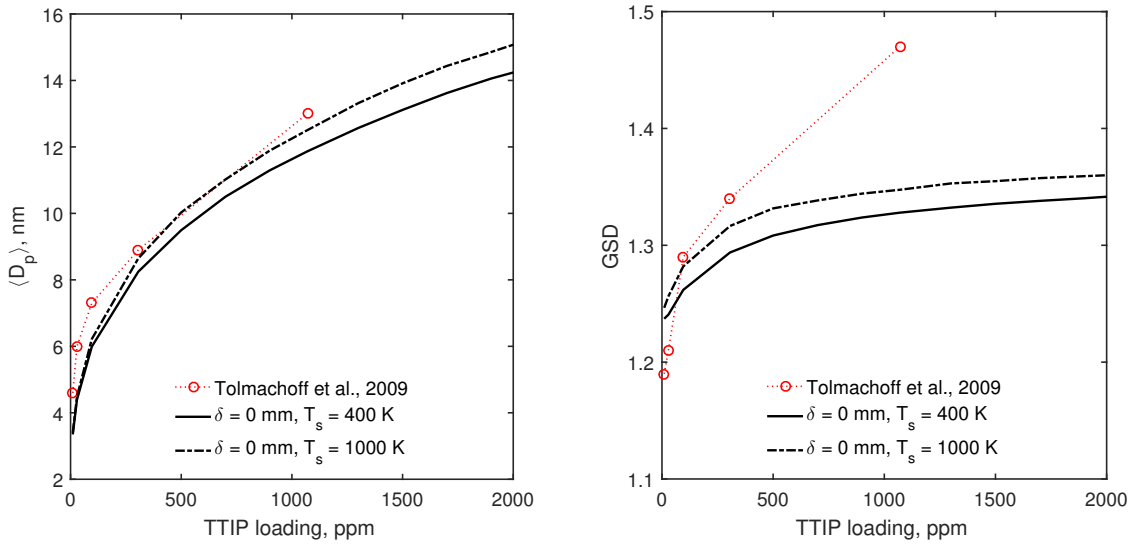

(a) log-Normal median particle size, $\langle D_p \rangle$.

(b) log-Normal geometric standard deviation, GSD.

Figure 5: Simulated median and GSD ($H = 1.27$ cm) as function of TTIP loading and surface temperature, T_s at stagnation plate, i.e. $\delta = 0$. Experimental data [14] ($L = 3.4$ cm) is shown as function of TTIP loading for stationary stagnation plate case.

Table 1: Simulated and experimental median size, $\langle D_p \rangle$, and geometric standard deviation, GSD, assuming $T_s = 1000$ K. (experimental data is taken from Tolmachoff et al. [14])

TTIP	Experimental data		Simulation result	
(ppm)	$\langle D_p \rangle$, nm	GSD	$\langle D_p \rangle$, nm	GSD
10	4.6	1.19	3.4	1.25
29	6.0	1.21	4.5	1.26
96	7.3	1.29	6.2	1.28
306	8.9	1.34	8.6	1.32
1070	13.0	1.47	12.5	1.35

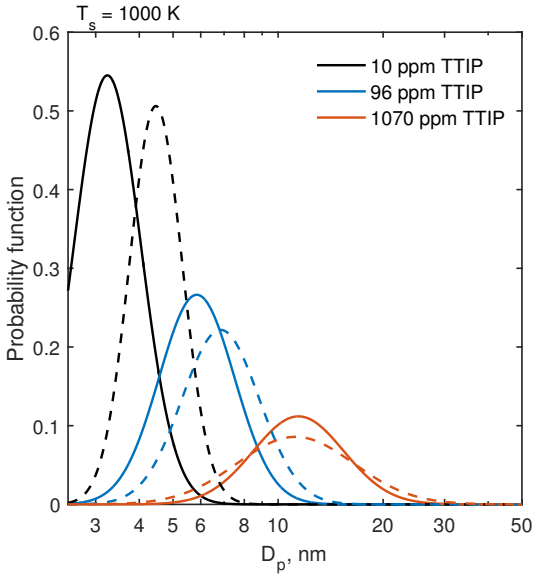

Figure 6: Log-Normal probability functions for model prediction (solid lines) and experimental data (dashed lines) for varying TTIP loading. The large apparent shift in low TTIP loading case is caused by the log-scaling of the x-axis.

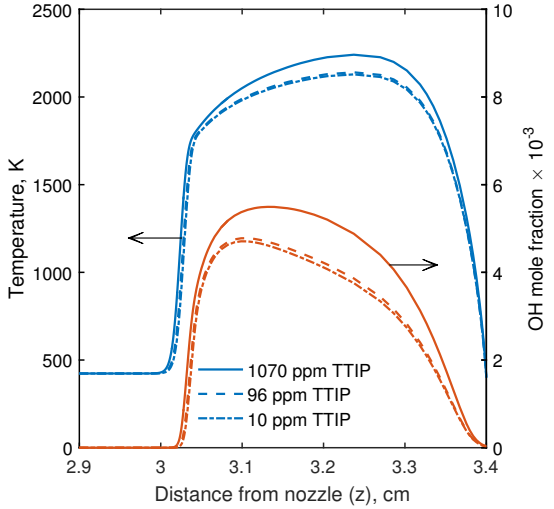

(a) Temperature and OH* mole fraction profiles.

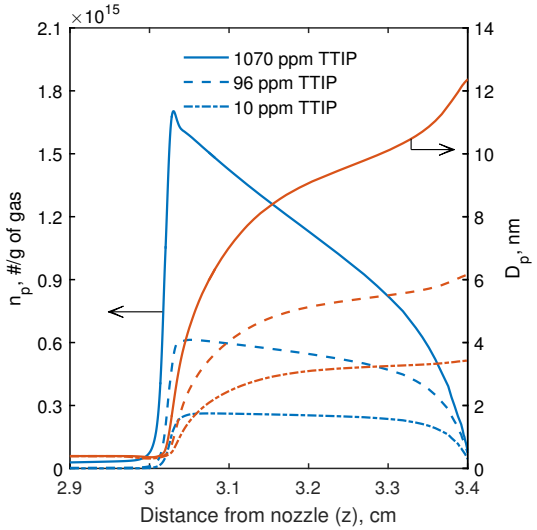

(b) Mean particle size, D_p, and particle number concentration, n_p, evolution along the flame.

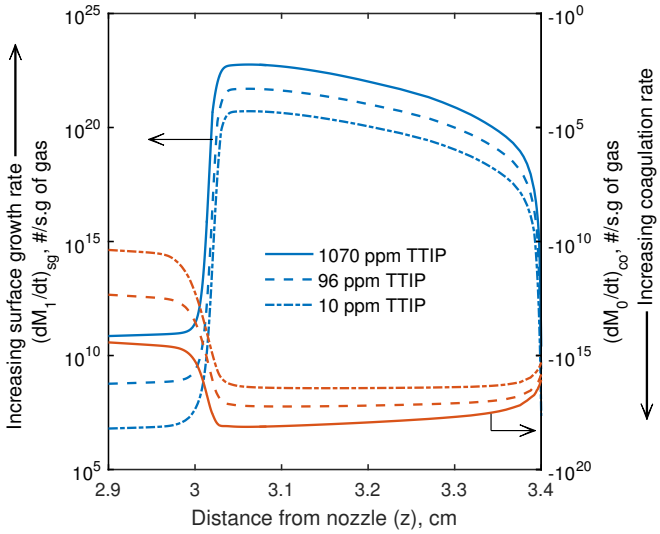

(c) Steady-state source terms for M_0 due to coagulation and M_1 due to surface growth.

Figure 7: Simulation results with varying precursor loading (10, 96, 1070 ppm TTIP, $H = 1.27$ cm).

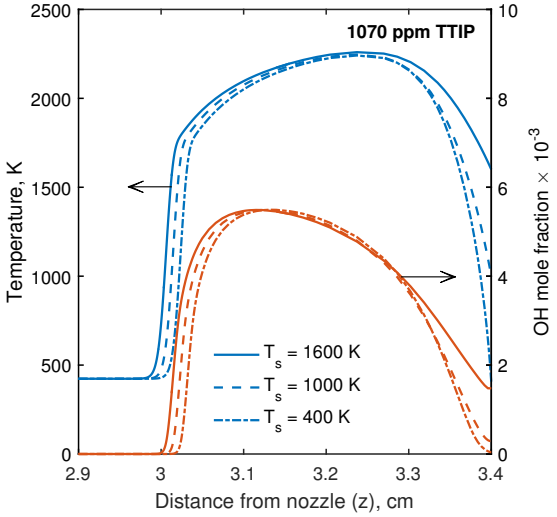

(a) Temperature and OH* mole fraction profiles.

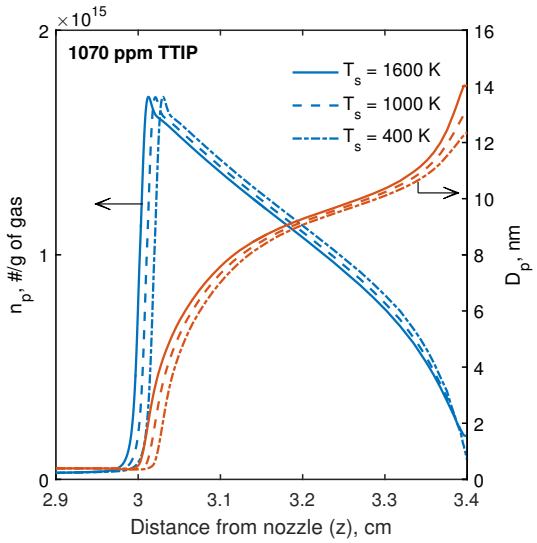

(b) Mean particle size, D_p, and particle number concentration, n_p, evolution along the flame.

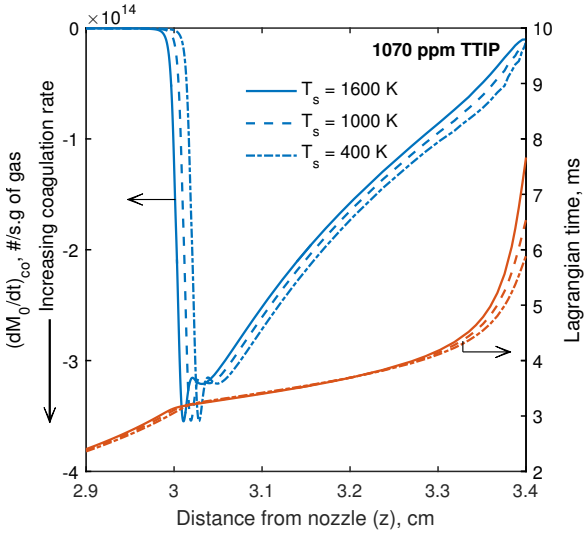

(c) Steady-state source terms for M_0 due to coagulation and calculated Lagrangian particle time.

Figure 8: Simulation results with varying stagnation temperature, T_s (400, 1000, and 1600 K), with $H = 1.27$ cm.

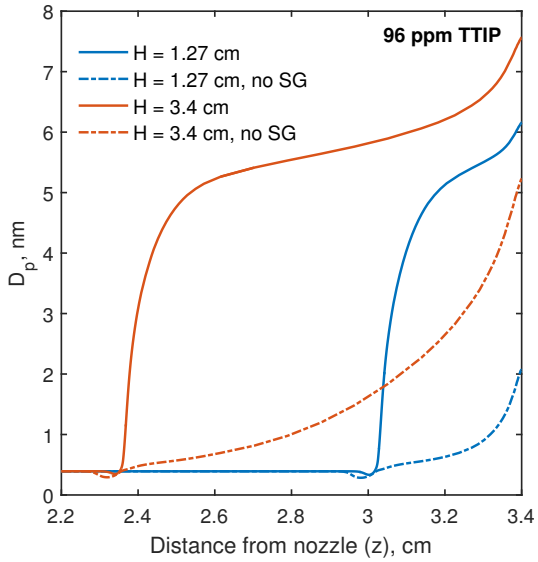

(a) Mean particle size, D_p, evolution along the flame.

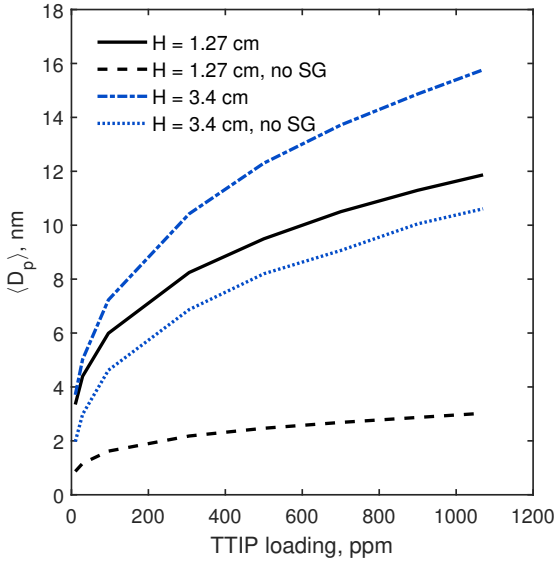

(b) Median particle size, D_p, at the stagnation surface as function of TTIP loading.

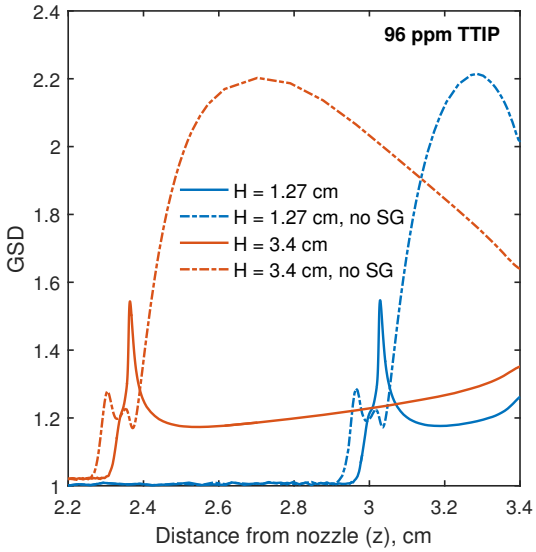

(c) Geometric standard deviation, GSD, evolution along the flame.

Figure 9: Simulation results with and without surface growth with nozzle-stagnation surface separation distance, H, of 1.27 and 3.4 cm.